# An Efficient Ray-Based Modeling Approach for Scattering From Reconfigurable Intelligent Surfaces

Enrico Maria Vitucci, *Senior Member, IEEE*, Matteo Albani, *Fellow, IEEE*, Silvi Kodra, Marina Barbiroli, and Vittorio Degli-Esposti, *Senior Member, IEEE*

***Abstract*— Reconfigurable intelligent surfaces (RISs), which can be implemented using metasurface technology or reflect/transmit antenna array technology, have garnered significant attention in research studies focused on both their technological aspects and potential applications. While various modeling approaches have been proposed—ranging from electromagnetic simulations and analytical integral formulations to simplified approaches based on scattering matrix theory—there remains a great need for efficient and electromagnetically consistent macroscopic models that can accurately simulate scattering from RISs, particularly for realistic simulations of RIS-based wireless networks. Building on previous work based on the characterization of the RIS through a surface impedance (or "spatial modulation") function and a few parameters, in the present article we propose a fully ray-based approach for the computation of the re-radiated field that can be easily embedded in efficient, forward ray tracing (also known as "ray launching") models. We validate the proposed model by comparison to well-established methods available in the literature. Results show that, although the considered method is based on a completely different formulation and is much more efficient than integral formulation methods, results are almost indistinguishable in some benchmark cases.**

***Index Terms*— Macroscopic modeling, metasurface, ray launching, ray tracing, reconfigurable intelligent surface (RIS).**

## I. Introduction

UNTIL recently, the design of wireless systems has been based on a probabilistic approach where the propagation channel was considered a largely unknown, random process that engineers had to cope with during the design of transmitter and receiver chains or network architecture. In the last years, Reconfigurable Intelligent Surface (RIS) technology has been proposed as an opportunity to broaden the design approach, allowing for the first time to engineer the wireless propagation channel. Interesting applications for 6G networks are envisioned to ease coverage limitations at mm-wave and THz frequencies and to perform basic operations on the signal "at the speed of light," limiting therefore the use of active repeaters and digital signal processing, with a reduction in latency and energy consumption [1].

An RIS is an electrically thin slab that can be realized either as a metasurface using electrically small, printed scattering elements, or as a reflect-array or a transmit-array with half-wavelength spaced printed antenna elements. Using control networks employing p-i-n diodes, varactors, or other methods, an RIS can dynamically tailor its local reflection or transmission properties and therefore can manipulate the reradiated field characteristics and wavefront shape [1], [2].

The scattering behavior of an RIS can be accurately simulated using *microscopic modeling* approaches (e.g., using Electromagnetic simulation or microwave network theory), that are based on a detailed description of the RIS microstructure. Unfortunately, microscopic models are complicated to use and require considerable computational resources. Therefore, they cannot be used for efficient, large-scale simulation of wireless links or systems employing RIS technology [3], [4].

Thus, path-loss models or channel models for RIS-assisted links have been developed and used for performance evaluations in recent years, see for example [5], [6], [7]. Such models however, being based on a discrete periodic approach that assumes independent scattering elements (unit cells) characterized by a given scattering coefficient and pattern, either overlook or only approximately take into account coupling, parasitic modes, and other nonidealities [3].

Several other approaches have been proposed in the literature to try to solve the above-mentioned limitations and to achieve a good trade-off between good electromagnetic consistency and low computational complexity. Some Authors propose hybrid approaches where electromagnetic simulation is used to derive a far-field radar cross section of the RIS to be inserted in ray tracing simulation [8]. Such approaches, although efficient, cannot be used to model near-field effects

Manuscript received 22 May 2023; revised 5 January 2024; accepted 15 January 2024. Date of publication 2 February 2024; date of current version 7 March 2024. This work was supported in part by the European Union under the Italian National Recovery and Resilience Plan (NRRP) of NextGenerationEU, Partnership on "Telecommunications of the Future" (PE00000001-program "RESTART")-Focused Project MOSS; in part by the Eu Project 6G SHort range extreme communication IN Entities (6G-SHINE), Horizon Europe Program, under Grant 101095738; and in part by the Eu COST Action Intelligence-Enabling Radio Communications for Seamless Inclusive Interactions (INTERACT) under Grant CA20120. *(Corresponding author: Enrico Maria Vitucci.)*

Enrico Maria Vitucci, Silvi Kodra, Marina Barbiroli, and Vittorio Degli-Esposti are with the Department of Electrical, Electronic, and Information Engineering "Guglielmo Marconi" (DEI), CNIT, University of Bologna, 40126 Bologna, Italy (e-mail: enricomaria.vitucci@unibo.it; silvi.kodra2@unibo.it; marina.barbiroli@unibo.it; v.degliesposti@unibo.it).

Matteo Albani is with the Department of Information engineering and mathematics, University of Siena, 53100 Siena, Italy (e-mail: matteo.albani@unisi.it).

Color versions of one or more figures in this article are available at https://doi.org/10.1109/TAP.2024.3359288.

Digital Object Identifier 10.1109/TAP.2024.3359288

such as focusing, which represents one of the most important RIS applications. Very promising are *macroscopic modeling* approaches that overlook the microscopic structure of the RIS in order to directly address the specific wave transformation it realizes [9], [10], [11], [12], [13]. These approaches assume that the metasurface can be homogenized and described in terms of an effective surface function– -e.g., a surface impedance or a surface (or spatial) modulation function—that determines such a wave transformation based on Maxwell's equations. The function can be derived from theory, i.e., from the wave transformation the RIS is intended to realize, or from experiment, i.e., from measurements on the wave transformation that an existing RIS actually realizes.

In particular, in [13], a realistic macroscopic model for evaluating multimode reradiation from generic, finite-size RIS is introduced. The model is based on a hybrid approach combining a Huygens-based method to model anomalously reradiated modes with well-established ray-based methods to model specular reflection and diffuse scattering that are inevitably present in real-world nonideal metasurfaces. In particular, diffuse scattering can model the noise-like reradiation effect of mechanical and electrical nonidealities such as deviation of the RIS from a flat surface, phase-tuning errors, or even phase-discretization effects due to the use of a limited number of bits in the control circuit. Specifically, the Huygens-based and the ray-based methods are combined through a parametric power-balance constraint that ensures energy conservation between the incident field, scattered field, and dissipation inside the slab.

In the present work, we build on the foregoing macroscopic and parametric approach to develop a ray-based, efficient approach also for anomalous reradiation, therefore achieving a fully-ray based macroscopic RIS model that can be easily integrated into efficient ray-launching (RL) algorithms for large-scale simulation such as the one proposed in [14]. In particular, we suitably extend geometrical optics (GO) theory [15] to the case of a reflective RIS illuminated with an astigmatic wavefront. Diffraction is modeled through the uniform geometrical theory of diffraction (UTD) [16], [17], and a new formulation of the UTD diffraction coefficients is proposed that can be applied to any reradiation mode of a RIS and easily implemented in RL tools, following the same approach of [17].

Differently from the study in [18], where a ray-based description of reradiation from locally periodic, finite metasurfaces was first proposed, we assume to model reradiation with a forward ray tracing approach, therefore avoiding the complex and time-consuming *critical point* search step.

In Section II of this article, we describe our approach more in detail, briefly addressing the model's parametric foundation, which is shared with the model described in [13], some basic concepts of GO that we have used, and then describing how the ray reradiated from a generic surface location (*anomalously reflected ray*) or from the surface edge (*anomalously diffracted ray*) are computed in terms of direction and field. The model is then validated in Section III by comparison with some reference models available in the literature.

## II. Proposed Approach

We propose a macroscopic, ray-based approach that uses the *spatial modulation function* introduced in [3] and [13], to model RIS reradiation. In the following, we make use of GO concepts such as ray, locally plane wave, local wavefront curvature, and spreading factor. [15]. In [18] and [12], an image-ray tracing approach for locally periodic metasurfaces is proposed, where "critical points" are identified using an iterative procedure, in order to trace reflected or transmitted rays for specific transmitter and receiver positions. In the present work, we propose a discrete RL approach where the RIS is discretized into surface elements, rays are launched toward each one of them, reflected/diffracted according to the spatial modulation function at the considered position, and re-launched in space without any need for a critical-point search phase. Therefore, the method can be inserted into a discrete, parallelized RL algorithm as the one presented in [14] for efficient field-prediction over an area or volume: in this case, the sub-set of RIS-reradiated rays hitting the desired target area or volume will have to be determined and their field can be mapped onto the target domain using some efficient computer graphics method. Surface discretization resolution, i.e., the size of each surface element (or "tile"), determines the spacing of the rays and therefore the resolution of the computed field, similar to what shown in [19, Fig. 4], for the traditional discrete ray launching model therein described, and should be therefore chosen according to a trade-off between accuracy and computation speed. However, discrete RL computation time can be drastically reduced using parallelization techniques [14], [19]. In this work, we leverage the macroscopic approach presented in [13], Section II, but we propose a more efficient, fully ray-based reradiated-field computation method in place of the Huygens-based methods there described. The basic assumptions, as in [13], are the following.

1) The homogenized surface properties vary slowly at the wavelength scale (slowly modulated RIS).
2) Because of 1), we use the concept of spatial modulation coefficient (SMC) often called also "reflection coefficient."
3) The reradiated field can be described as a discrete set of reradiation modes (e.g., Floquet's modes of a locally periodic metasurface).
4) We address the computation of radiative near field and far-field, but we neglect for the time being the effect of evanescent modes (i.e., surface waves) and vertex diffraction.

On the base of the foregoing assumptions, we describe each reradiating mode field as a set of rays reflected or diffracted at each surface element. In the rest of this section, after recalling basic GO concepts, the computation of:

1) reradiation angle;
2) field;
3) spreading factor.

Is described as a reflected or edge-diffracted ray of a single re-radiation mode. For a complete field computation, the procedure will have to be iterated for all the propagating modes.

For the sake of brevity, only reflecting RISs are considered: although the extension to *transmissive* RISs, that reradiate mainly in the forward half-space, is quite straightforward, it will be addressed in future work.

### A. Relevant GO Background

According to GO theory, a propagating wave in free space can be described in terms of rays, i.e., lines that are everywhere orthogonal to the wavefront and therefore represent wave *paths*. In the high-frequency regime, the Electromagnetic field of a propagating wave can be approximated as [15]

$$\begin{aligned}\mathbf{E}(\mathbf{r}) &\simeq \mathbf{E}_0(\mathbf{r})e^{-jk_0\psi(\mathbf{r})}\\ \mathbf{H}(\mathbf{r}) &\simeq \mathbf{H}_0(\mathbf{r})e^{-jk_0\psi(\mathbf{r})}\end{aligned} \tag{1}$$

where $\mathbf{r}$ is the position vector of the generic observation point P, $k_0 = 2\pi c_0/f$ is the free space wavenumber, $\mathbf{E}_0(\mathbf{r})$, $\mathbf{H}_0(\mathbf{r})$ are slowly varying complex vectors, representing the local amplitude and polarization of the wave, and $\psi(\mathbf{r})$, also called eikonal function, is an optical-length function that depends on the actual shape of the wavefront. In particular, the gradient of the eikonal function $\nabla\psi$, is normal to the wavefront and then defines the local ray direction, while the Hessian matrix of $\psi$, indicated as $\nabla\nabla\psi$, takes into account the local curvature of the wavefront. The Hessian matrix of the eikonal function is often indicated with the symbol $\underline{\mathbf{Q}}$ and called the *curvature matrix* of the local wavefront [20], [21]. By substituting (1) in Maxwell's equations, the following relations are obtained (*locally plane* TEM wave) [15]:

$$\nabla\psi\cdot\mathbf{E}=0 \quad \nabla\psi\cdot\mathbf{H}=0 \;\; \eta\mathbf{H}=\nabla\psi\times\mathbf{E} \tag{2}$$

where $\eta = \sqrt{\mu_0/\epsilon_0}$ is the free-space impedance, and the symbols "$\cdot$" and "$\times$" stand for the dot scalar product and the cross vector product, respectively. Moreover, it can be proved that in a homogeneous medium, the ray trajectories are rectilinear. In particular, in free space, the generic ray has constant direction $\hat{\mathbf{s}} = \nabla\psi$, whereas the wavefront has an astigmatic shape so that the $E$-field propagating along a single ray can be written as [20]

$$\begin{aligned}\mathbf{E}(s) &= \mathbf{E}(0)A(s)e^{-jk_0 s}\\ &= \mathbf{E}(0)\sqrt{\frac{\text{pdet}\left\{\underline{\mathbf{Q}}(s)\right\}}{\text{pdet}\left\{\underline{\mathbf{Q}}(0)\right\}}}\,e^{-jk_0 s}\end{aligned} \tag{3}$$

where $s$ is the local coordinate along the ray, i.e., the distance between the current point and the reference point $s = 0$, $\mathbf{E}(0)$ is the field at the reference point, and $A(s) = \sqrt{\text{pdet}\{\underline{\mathbf{Q}}(s)\}/\text{pdet}\{\underline{\mathbf{Q}}(0)\}}$ is the so-called *spreading (or divergence) factor*, that derives from power conservation on a ray tube and depends on the actual wavefront's shape. In (3), the notation pdet{$-$} stands for the *pseudo-determinant* of the square matrix, i.e., the product of its non-zero eigenvalues.

The curvature matrix of an astigmatic wave can be expressed in the following way [17], [20]:

$$\underline{\mathbf{Q}}(s) = \frac{1}{\rho_1+s}\hat{\mathbf{X}}_1\hat{\mathbf{X}}_1 + \frac{1}{\rho_2+s}\hat{\mathbf{X}}_2\hat{\mathbf{X}}_2 \tag{4}$$

with $\rho_1$ and $\rho_2$ being the principal curvature radii at the reference point, corresponding to the two principal curvature directions $\hat{\mathbf{X}}_1, \hat{\mathbf{X}}_2$. In (4) and in the following, the dyadic product is used for ease of notation, which is equivalent in linear algebra to the multiplication of a column vector by a row vector, i.e.,

$$\mathbf{ab} \equiv \mathbf{ab}^T$$

where the superscript $()^T$ stands for the transpose operator.

According to (4), in free space, the wavefront diverges as it propagates without changing shape, i.e., the two principal directions remain the same while the curvature radii linearly increase with $s$ as $\rho_1 + s$ and $\rho_2 + s$.

By definition (4), $\underline{\mathbf{Q}}(s)$ is a rank-2 symmetric matrix, and the wave principal curvatures $\kappa_1 = (\rho_1+s)^{-1}$, $\kappa_2 = (\rho_2+s)^{-2}$ are its nonzero eigenvalues, while the principal directions $\hat{\mathbf{X}}_1, \hat{\mathbf{X}}_2$ are the corresponding eigenvectors. This means that, by adopting the local ray-fixed reference system $(\hat{\mathbf{X}}_1, \hat{\mathbf{X}}_2, \hat{\mathbf{s}})$, $\underline{\mathbf{Q}}(s)$ is diagonalized in the form

$$\underline{\mathbf{Q}}(s) = \begin{bmatrix}\frac{1}{\rho_1+s} & 0 & 0\\ 0 & \frac{1}{\rho_2+s} & 0\\ 0 & 0 & 0\end{bmatrix}. \tag{5}$$

As a consequence of (4), (5) the following property holds, as the principal directions $\hat{\mathbf{X}}_1, \hat{\mathbf{X}}_2$ lay on the transverse plane with respect to the ray direction $\hat{\mathbf{s}}$

$$\underline{\mathbf{Q}}\,\hat{\mathbf{s}} = \hat{\mathbf{s}}^T\underline{\mathbf{Q}} = \mathbf{0}. \tag{6}$$

Finally, according to (3) and (5), the spreading factor for an astigmatic wave can be expressed as a function of the principal curvature radii in the form

$$A(s) = \sqrt{\frac{\rho_1\rho_2}{(\rho_1+s)(\rho_2+s)}}. \tag{7}$$

As it can be seen from (7), the GO field has singularities on the wave *caustics*, i.e., for those points along rays so that $s = -\rho_1$ or $s = -\rho_2$. GO theory cannot be applied to compute the field in the vicinity of a caustic: in such a case, different methods based on asymptotic evaluation need to be applied [22].

In the following, according to the GO approach, we leverage the locally plane wave assumption to model reflection and diffraction at each surface element of a RIS, while we account for the wavefront's actual shape through the spreading factor, that gives the actual attenuation-trend of field's intensity with distance. In practice, we linearize both the incident wavefront - with a local plane—and the effect of the RIS on it—with the local phase gradient—in order to simplify computation steps (i) and (ii) above, whereas the actual curvatures of the wavefront are considered for step (iii).

### B. Anomalous Ray Reflection

Anomalous ray reflection is modeled according to a 3D version of the *generalized law of reflection* [23], which takes into account that, in general, incidence plane and reflection

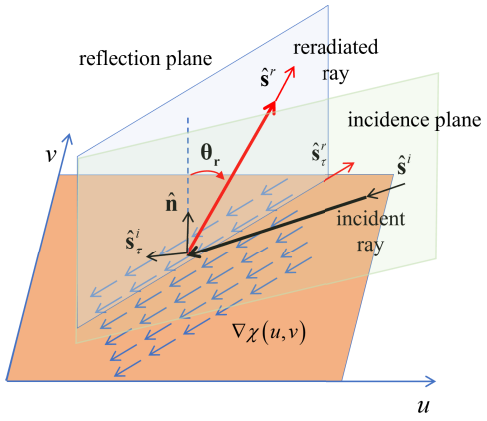


Fig. 1. Total phase gradient and anomalous ray reflection at the generic surface element.

plane can be different. For the sake of simplicity, we limit the analysis to flat surfaces, but the extension to the case of a curved RIS is possible.

Let us then consider a flat RIS of normal $\hat{\mathbf{n}}$, and let be $\mathbf{r}'$ the position of the generic surface element. The position vector can be expressed as a function of 2 local coordinates on the RIS plane (see Fig. 1), i.e., $\mathbf{r}' = \mathbf{r}'(u, v)$. When a ray impinges on the surface with propagation direction $\hat{\mathbf{s}}^i$ so that $-\hat{\mathbf{s}}^i \cdot \hat{\mathbf{n}} = \cos\theta_i$, where $\theta_i$ is the incidence angle, the field acquires an *incidence phase gradient* on the surface due to the inclination of the locally-plane wavefront of the ray with respect to the RIS. This phase gradient is

$$\nabla\chi^{\,i} = -k_0 \sin\theta_i \, \hat{\mathbf{s}}^i_\tau \tag{8}$$

where the unit vector $\hat{\mathbf{s}}^i_\tau$ defines the orientation of the incidence plane with respect to the RIS surface (see Fig. 1).

Equation (8) can be rewritten in the equivalent form

$$\underline{\mathbf{P}}_\tau \, \hat{\mathbf{s}}^i = \hat{\mathbf{s}}^i - \hat{\mathbf{n}}\left(\hat{\mathbf{n}} \cdot \hat{\mathbf{s}}^i\right) = \sin\theta_i \, \hat{\mathbf{s}}^i_\tau = -\frac{\nabla\chi^{\,i}}{k_0} \tag{9}$$

where $\underline{\mathbf{P}}_\tau$ is the tangent projection operator, defined as

$$\underline{\mathbf{P}}_\tau = \underline{\mathbf{1}} - \hat{\mathbf{n}}\hat{\mathbf{n}} \tag{10}$$

and $\underline{\mathbf{1}}$ is the identity matrix.

Then, according to a macroscopic approach, the RIS applies the additional phase gradient $\nabla\chi^m$ of the considered reradiation mode so that the *total phase gradient* at the considered surface location becomes

$$\nabla\chi = \nabla\chi^{\,i} + \nabla\chi^m \tag{11}$$

Anomalous reflection direction takes place according to that total phase gradient. The reflection plane is parallel to the phase gradient direction (see Fig. 1); however, as surface points with a greater phase will reradiate before those with a phase lag, the resulting locally-plane wavefront will have the opposite orientation with respect to the total phase gradient $\nabla\chi$. It can be easily shown (see Appendix I) that the projection of the reflected ray direction on RIS plane is given by

$$\underline{\mathbf{P}}_\tau \, \hat{\mathbf{s}}^r = \sin\theta_r \, \hat{\mathbf{s}}^r_\tau = \underline{\mathbf{P}}_\tau \, \hat{\mathbf{s}}^i - \frac{\nabla\chi^m}{k_0} = -\frac{\nabla\chi}{k_0} \tag{12}$$

where $\theta_r$ is the reradiation angle, and $\hat{\mathbf{s}}^r_\tau$ defines the reflection (or reradiation) plane, that generally for a RIS is different from the incidence plane, as shown in Fig. 1.

Observing that $|\hat{\mathbf{s}}^r| = 1$, the reflection unit vector can be written using a single compact equation

$$\begin{aligned}\hat{\mathbf{s}}^r &= \underline{\mathbf{P}}_\tau \, \hat{\mathbf{s}}^i - \frac{\nabla\chi^m(\mathbf{r}')}{k_0} + \sqrt{1 - \left|\underline{\mathbf{P}}_\tau \, \hat{\mathbf{s}}^i - \frac{\nabla\chi^m(\mathbf{r}')}{k_0}\right|^2} \;\; \hat{\mathbf{n}} \\ &= -\frac{\nabla\chi(\mathbf{r}')}{k_0} + \sqrt{1 - \left|\frac{\nabla\chi(\mathbf{r}')}{k_0}\right|^2} \;\; \hat{\mathbf{n}}\end{aligned} \tag{13}$$

which expresses the *generalized law of reflection*.

As in [3] and [13], the reradiated field can be computed using the SMC, that takes into account the overall reradiation properties of the RIS. According to this macroscopic approach, we assume that the following boundary condition holds for every point of the RIS surface:

$$\mathbf{E}^r(\mathbf{r}') = \underline{\Gamma}(\mathbf{r}')\mathbf{E}^i(\mathbf{r}'). \tag{14}$$

In (14), instead of a scalar coefficient we make use of the coefficient $\underline{\Gamma}$ written in dyadic form, in order to take into account the polarimetric effect of the RIS. Such coefficient is defined as

$$\begin{aligned}\underline{\Gamma}(\mathbf{r}') &= \underline{\Gamma}_0(\mathbf{r}')\mathrm{e}^{j\chi^m(\mathbf{r}')} = A^m(\mathbf{r}')\mathrm{e}^{j\chi^m(\mathbf{r}')} \cdot \underline{\mathbf{R}}^m \\ &= A^m(\mathbf{r}')\mathrm{e}^{j\chi^m(\mathbf{r}')} \cdot \left(R^m_\parallel \, \hat{\mathbf{e}}^i_\parallel \hat{\mathbf{e}}^r_\parallel + R^m_\perp \, \hat{\mathbf{e}}^i_\perp \hat{\mathbf{e}}^r_\perp\right)\end{aligned} \tag{15}$$

where $A^m$ and $\chi^m$ are the amplitude and phase modulation of the considered reradiation mode, while the matrix $\underline{\mathbf{R}}^m = R^m_\parallel \, \hat{\mathbf{e}}^i_\parallel \hat{\mathbf{e}}^r_\parallel + R^m_\perp \, \hat{\mathbf{e}}^i_\perp \hat{\mathbf{e}}^r_\perp$ is used to account for the polarization transformation realized by the RIS [17], [24]. The unit vectors $\hat{\mathbf{e}}^{i,r}_\perp$ and $\hat{\mathbf{e}}^{i,r}_\parallel$ are used to decompose the incident/reflected field into perpendicular (TE) and parallel (TM) components with respect to the incidence/reflection plane on a ray-fixed reference system (see Fig. 1), and are easily computed as

$$\hat{\mathbf{e}}^{i,r}_\perp = \hat{\mathbf{s}}^{i,r}_\tau \times \hat{\mathbf{n}} \qquad \hat{\mathbf{e}}^{i,r}_\parallel = \hat{\mathbf{e}}^{i,r}_\perp \times \hat{\mathbf{s}}^{i,r}. \tag{16}$$

Usually, the phase modulation coefficient $\chi^m$ varies on the wavelength scale, while the amplitude modulation coefficient $A^m$ varies on a larger scale and may take into account nonlocal effects along the RIS surface. In general, $A^m$ and $\chi^m$ cannot be arbitrarily chosen but must satisfy proper constraints in order to be representative of a realistic RIS design, as discussed in detail in [3]. A RIS able to control the polarization, here modeled through the dyadic $\underline{\mathbf{R}}^m$, can be alternatively represented as a tensor impedance sheet (see for example [25, pp. 57–59]). Additional terms may be introduced in (15) to take into account additional losses caused by parasitic effects and diffuse scattering, as discussed in [13]. In the following, we assume that the SMC $\underline{\Gamma}$ is known, either from the design stage or estimated through measurements.

After defining the local reflection direction $\hat{\mathbf{s}}^r$ and applying the SMC to the incident field, the last step consists in the computation of the field along the reflected ray, including the spreading factor. This can be derived through the curvature matrix by applying a local phase matching procedure on the RIS surface, following a method similar to the one presented in [20], and also used in [17] to derive the spreading factor

of the reflected wave from a curved PEC surface. Differently from [20], here we express wave curvatures using $3 \times 3$ non-diagonal curvature matrices, avoiding the use of a ray-fixed local reference system on the incident and reflected wave to diagonalize them, that would need multiple matrix transformations. As a starting point, by substituting (1) and (15) in (14), we get

$$\mathbf{E}_0^r(\mathbf{r}')e^{-jk_0\psi^r(\mathbf{r}')} = \underline{\Gamma}_0(\mathbf{r}')\mathbf{E}_0^i(\mathbf{r}')e^{j[\chi^m(\mathbf{r}')-k_0\psi^i(\mathbf{r}')]} \tag{17}$$

and then

$$\mathbf{E}_0^r(\mathbf{r}') = \underline{\Gamma}_0(\mathbf{r}')\mathbf{E}_0^i(\mathbf{r}') \tag{18a}$$

$$k_0\psi^r(\mathbf{r}') = k_0\psi^i(\mathbf{r}') - \chi^m(\mathbf{r}') \tag{18b}$$

Equation (18b) is a phase-matching relation that involves the phase of incident and reflected fields, and the phase $\chi^m$ imposed by the RIS. By expressing each phase term through its Taylor series expansion about a reference point $\mathbf{r}_0'$ on the RIS, a simple relation between the local curvature matrices of the incident and reflected fields can be derived, as shown in Appendix I

$$\mathbf{t}\cdot\underline{\mathbf{Q}}^r\mathbf{t} = \mathbf{t}\cdot\left\{\left[\underline{\mathbf{Q}}^i - \frac{1}{k_0}\nabla\nabla\chi^m(\mathbf{r}_0')\right]\mathbf{t}\right\} \tag{19}$$

where $\mathbf{t} = \mathbf{r}' - \mathbf{r}_0'$ is any vector tangent to the RIS surface at $\mathbf{r}_0'$, and $\nabla\nabla\chi^m$ is the Hessian matrix of the phase profile $\chi^m$ imposed by the RIS, computed in $\mathbf{r}_0'$.

In order for (19) to be satisfied, the tangent projection of the incident curvature matrix, plus the curvature imposed by the RIS, must equate the tangent projection of the reflected curvature matrix, i.e.,

$$\underline{\mathbf{P}}_\tau\underline{\mathbf{Q}}^r\underline{\mathbf{P}}_\tau = \underline{\mathbf{P}}_\tau\left[\underline{\mathbf{Q}}^i - \frac{1}{k_0}\nabla\nabla\chi^m\right]\underline{\mathbf{P}}_\tau. \tag{20}$$

Equation (20) only provides the tangential component of $\underline{\mathbf{Q}}^r$. The normal component is determined by imposing (6) for the reflected ray, i.e.,

$$\underline{\mathbf{Q}}^r\,\hat{\mathbf{s}}^r = \mathbf{0}.$$

In particular, by combining (6) and (20), through simple algebraic manipulations the final expression of $\underline{\mathbf{Q}}^r$ can be found

$$\underline{\mathbf{Q}}^r = \underline{\mathbf{L}}^T\left[\underline{\mathbf{Q}}^i - \frac{1}{k_0}\nabla\nabla\chi^m\right]\underline{\mathbf{L}} \tag{21}$$

where $\underline{\mathbf{L}}$ is a linear transformation operator, having the following form:

$$\underline{\mathbf{L}} = \left(\underline{\mathbf{1}} - \frac{\hat{\mathbf{s}}^r\,\hat{\mathbf{n}}}{\hat{\mathbf{s}}^r\cdot\hat{\mathbf{n}}}\right). \tag{22}$$

According to GO rules, after reflecting on the RIS the wave continues to propagate along a rectilinear trajectory and the curvature radii increase proportionally to the path length, as the medium above the RIS surface is homogeneous. If the incident ray hits the RIS in the point $\mathbf{r}'$, the GO field on a observation point $\mathbf{r} = \mathbf{r}' + s\,\hat{\mathbf{s}}^r$ along the reflected ray is then expressed by

$$\begin{aligned}\mathbf{E}^r(\mathbf{r}) &= \underline{\Gamma}(\mathbf{r}')\mathbf{E}^i(\mathbf{r}')A^r(s)\,e^{-jk_0|\mathbf{r}-\mathbf{r}'|}\\ &= \underline{\Gamma}(\mathbf{r}')\mathbf{E}^i(\mathbf{r}')\sqrt{\frac{\rho_1^r\rho_2^r}{(\rho_1^r+s)(\rho_2^r+s)}}\,e^{-jk_0s}\end{aligned} \tag{23}$$

with $\rho_1^r$, $\rho_2^r$ being the principal curvature radii of the reflected wave at $\mathbf{r}'$, i.e., the reciprocals of the nonzero eigenvalues of the reflection curvature matrix $\underline{\mathbf{Q}}^r$, computed through (21), and $s$ the local coordinate along the reflected ray.

It is worth noting that generally, according to (21), RIS reflection changes the wavefront shape into an astigmatic wave even in simple cases, like with a spherical wave incident on a constant phase gradient RIS, i.e., with $\nabla\nabla\chi^m = 0$. For instance, let us consider the case of an anomalous reflector configured with constant anomalous angle $\theta_r$, and reradiation plane coincident with the incidence plane (i.e., $\Delta\phi = 0$ in Fig. 1). If such a RIS is illuminated by a spherical wave, i.e., with $\rho_1^i = \rho_2^i = s'$, using (21) it can be easily shown that the reflected wave has curvatures $\rho_1^r = s'$ and $\rho_2^r = s'\cos^2\theta_r/\cos^2\theta_i$: the curvature perpendicular to the incidence plane is unchanged, while the one laying in the incidence plane is modified by anomalous reflection. Therefore, the spherical wavefront shape is unchanged only in the case of specular reflection.

### C. Anomalous Ray Diffraction

Besides the GO contributions for the RIS scattered field, edge diffracted ray-fields are also included in the model. This type of contribution is important to smooth out the abrupt field discontinuity predicted by GO when crossing the shadow boundaries and to predict a nonzero field in the GO shadow region. Since an exact solution for the truncated RIS canonical problem is not available, the edge diffracted field has to be evaluated by resorting to an approximate solution. Similar to the approach adopted for the diffraction from arbitrary impedance wedges, two methods are possible; one can either resort to a PO approximate formulation and derive ray contributions from its asymptotic evaluation [26], or develop heuristic solutions [27], [28] by modifying the UTD coefficient [17]. While in [18] the former methodology was pursued, here we follow the latter which is more popular and effective for the application to ray-tracing and propagation prediction because of its simplicity. Since the total phase progression along the RIS edges results from the combination of both the incident wave illumination and the surface impedance modulation, edge diffracted rays are launched toward anomalous directions, similar to what happens for GO reflected rays.

Namely, according to a *generalized law of diffraction*, the diffracted ray direction $\hat{\mathbf{s}}^d$ must obey to (see Appendix II for the proof)

$$\begin{aligned}\cos\beta &= \hat{\mathbf{s}}^d\cdot\hat{\mathbf{e}} = \hat{\mathbf{s}}^r\cdot\hat{\mathbf{e}}\\ &= \left(\hat{\mathbf{s}}^i - \frac{\nabla\chi^m}{k_0}\right)\cdot\hat{\mathbf{e}} = \cos\beta' - \frac{1}{k_0}\frac{\partial\chi^m}{\partial e}\end{aligned} \tag{24}$$

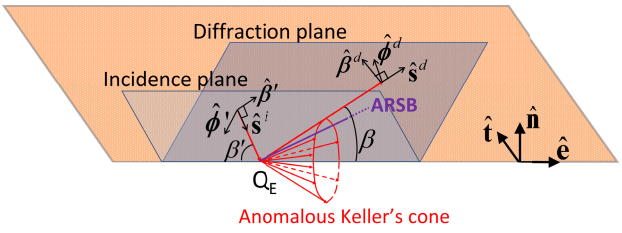


Fig. 2. Anomalous Keller's cone and edge-fixed reference system for incident and diffracted ray.

where $\beta$ is the aperture angle of the Keller-Rubinowicz diffraction cone, $\beta'$ is the incidence angle with respect to the edge and $\hat{\mathbf{e}}$ is the unit vector along the edge, as shown in Fig. 2.

Looking at (24), it is evident that the additional term corresponding to the spatial modulation modifies the cone aperture with respect to the standard case, thus leading to an *anomalous diffraction*. Moreover, the transverse component of the reflection direction $\hat{\mathbf{s}}^r$ with respect to the edge direction $\hat{\mathbf{e}}$ gives rise to an anomalous reflection shadow boundary (ARSB). This applies of course to any reradiation mode of the RIS.

Therefore, one can proceed similar to the standard UTD case, by recalling that the diffracted wave is astigmatic with one caustic on the edge, and that the diffracted field is computed as [17]

$$\mathbf{E}^d(s) = \underline{\mathbf{D}} \cdot \mathbf{E}^i(Q_E) \sqrt{\frac{\rho^d}{s\left(\rho^d + s\right)}}\, e^{-jk_0 s}. \tag{25}$$

In (25), $\underline{\mathbf{D}}$ is the dyadic diffraction coefficient, and $\rho^d$ is the edge-caustic distance, i.e., the distance between the caustic at the edge and the second caustic of the diffracted ray.

For a straight edge, $\rho^d$ is related to the incident wave curvature radius on the edge-fixed incidence plane, i.e., $\rho_e^i$, through the following equation (see Appendix II for the proof):

$$\frac{1}{\rho^d} = \frac{1}{\rho_e^i}\frac{\sin^2\beta'}{\sin^2\beta} - \frac{1}{k_0 \sin^2\beta}\frac{\partial^2 \chi^m}{\partial e^2}. \tag{26}$$

Looking at (26), it is evident that the curvature of the incident wave on the edge-fixed diffraction plane is modified by anomalous diffraction, similar to what happens for anomalous reflection. If the RIS has a constant phase gradient along the edge, such curvature $\rho^d$ is also constant along the edge.

Diffraction must also compensate for the incident field that vanishes at the incidence shadow boundary (ISB). However, the incident ray boundary is not modified by the surface impedance modulation of the RIS across the edge. This means that, in addition to the anomalous Keller's cone, also an *ordinary* Keller's cone of diffracted rays originates at the diffraction point $Q_E$ (see Fig. 3), i.e.,

$$\cos\beta' = \hat{\mathbf{s}}^i \cdot \hat{\mathbf{e}} = \hat{\mathbf{s}}^{do} \cdot \hat{\mathbf{e}} \tag{27}$$

with $\hat{\mathbf{s}}^{do}$ direction of the diffracted ray laying on the ordinary Keller's cone. For those diffracted rays, the incident field curvature is not modified by diffraction on a straight edge, i.e., $\rho^d = \rho_e^i$ [17].

Regarding the dyadic diffraction coefficient $\underline{\mathbf{D}}$ in (25), it is expressed as a combination of unit vectors parallel and perpendicular to the incidence and diffraction edge-fixed planes,

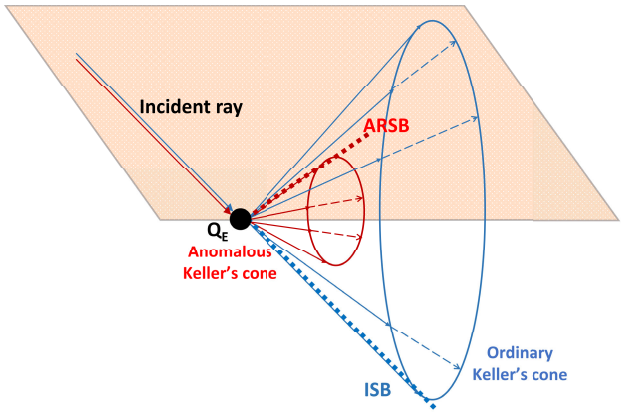


Fig. 3. Ordinary and anomalous Keller's cones for a given point along the edge.

as in [17]. However, different from the standard UTD, two separate diffraction coefficients are defined for the anomalous and ordinary diffracted rays. Therefore, we extend the formulation of the UTD diffraction coefficient to the case of a RIS in the following way:

$$\underline{\mathbf{D}}^i = D^i\left(-\hat{\boldsymbol{\beta}}\hat{\boldsymbol{\beta}}' - \hat{\boldsymbol{\phi}}\hat{\boldsymbol{\phi}}'\right) \tag{28}$$

$$\underline{\mathbf{D}}^r = \left(-D_s^r\, \hat{\boldsymbol{\beta}}^d\hat{\boldsymbol{\beta}}' - D_h^r\, \hat{\boldsymbol{\phi}}^d\hat{\boldsymbol{\phi}}'\right)\underline{\Gamma} \tag{29}$$

where $D^i$ is the scalar diffraction coefficient that applies to the diffracted rays on the ordinary Keller's cone, $D_s^r$ and $D_h^r$ are the "soft" and "hard" scalar diffraction coefficients [17] for the anomalous diffraction. In (29), $D_s^r$ and $D_h^r$ are also multiplied by the SMC $\underline{\Gamma}$ to properly compensate for anomalous reflection on the ARSB, following the heuristic approach adopted in [27] and [28] for a nonperfectly conducting wedge.

The unit vectors $(\hat{\boldsymbol{\phi}}', \hat{\boldsymbol{\beta}}')$ form a right-handed triplet with the incidence direction $\hat{\mathbf{s}}^i$ (see Fig. 2) and similarly, $(\hat{\boldsymbol{\phi}}, \hat{\boldsymbol{\beta}})$ and $(\hat{\boldsymbol{\phi}}^d, \hat{\boldsymbol{\beta}}^d)$ form a right-handed triplet with the ordinary and anomalous diffraction directions $\hat{\mathbf{s}}^{do}$ and $\hat{\mathbf{s}}^d$, respectively. Therefore, they are easily computed as

$$\begin{aligned}
\hat{\boldsymbol{\phi}}' &= -\frac{\hat{\mathbf{e}} \times \hat{\mathbf{s}}^i}{|\hat{\mathbf{e}} \times \hat{\mathbf{s}}^i|} & \hat{\boldsymbol{\phi}} &= \frac{\hat{\mathbf{e}} \times \hat{\mathbf{s}}^{do}}{|\hat{\mathbf{e}} \times \hat{\mathbf{s}}^{do}|} & \hat{\boldsymbol{\phi}}^d &= \frac{\hat{\mathbf{e}} \times \hat{\mathbf{s}}^d}{|\hat{\mathbf{e}} \times \hat{\mathbf{s}}^d|} \\
\hat{\boldsymbol{\beta}}' &= \hat{\boldsymbol{\phi}}' \times \hat{\mathbf{s}}^i & \hat{\boldsymbol{\beta}} &= \hat{\boldsymbol{\phi}} \times \hat{\mathbf{s}}^{do} & \hat{\boldsymbol{\beta}}^d &= \hat{\boldsymbol{\phi}}^d \times \hat{\mathbf{s}}^d.
\end{aligned} \tag{30}$$

In order to express the scalar diffraction coefficients $D^i$, $D_s^r$, $D_h^r$ in (28), (29) in a similar form to the one introduced in [17] for standard UTD, we need to define the ray angular coordinates with respect to the edge (see Figs. 2–4). They can be computed with the following equations [29]:

$$\beta = \arccos\left(\hat{\mathbf{s}}^r \cdot \hat{\mathbf{e}}\right) \tag{31}$$

$$\beta' = \arccos\left(\hat{\mathbf{s}}^i \cdot \hat{\mathbf{e}}\right) \tag{32}$$

$$\phi^d = \pi - \left[\pi - \arccos\left(\frac{\hat{\mathbf{s}}^d \cdot \hat{\mathbf{t}}}{\sin\beta}\right)\right]\mathrm{sgn}\left(\frac{\hat{\mathbf{s}}^d \cdot \hat{\mathbf{n}}}{\sin\beta}\right) \tag{33}$$

$$\phi'^r = \pi - \left[\pi - \arccos\left(\frac{-\hat{\mathbf{s}}^r \cdot \hat{\mathbf{t}}}{\sin\beta}\right)\right]\mathrm{sgn}\left(\frac{\hat{\mathbf{s}}^r \cdot \hat{\mathbf{n}}}{\sin\beta}\right) \tag{34}$$

$$\phi = \pi - \left[\pi - \arccos\left(\frac{\hat{\mathbf{s}}^{do} \cdot \hat{\mathbf{t}}}{\sin\beta'}\right)\right]\mathrm{sgn}\left(\frac{\hat{\mathbf{s}}^{do} \cdot \hat{\mathbf{n}}}{\sin\beta'}\right) \tag{35}$$

$$\phi' = \pi - \left[\pi - \arccos\left(\frac{-\hat{\mathbf{s}}^i \cdot \hat{\mathbf{t}}}{\sin\beta'}\right)\right]\mathrm{sgn}\left(\frac{-\hat{\mathbf{s}}^i \cdot \hat{\mathbf{n}}}{\sin\beta'}\right) \tag{36}$$

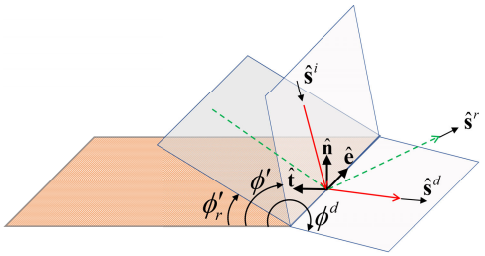


Fig. 4. Diffraction angles for anomalous diffraction. Red: incident ray and one anomalous diffracted ray with corresponding incidence and diffraction planes; Green: anomalous reflected ray and its opposite (back-specular) direction.

with $\hat{\mathbf{n}}$ denoting the unit vector normal to the RIS and $\hat{\mathbf{t}} = \hat{\mathbf{n}} \times \hat{\mathbf{e}}$ the unit vector tangent to the RIS and orthogonal to the edge.

Compared to the standard UTD, in (31)–(36) 3 additional angles are introduced, namely $\beta$, $\phi^d$ and $\phi'^r$: $\beta$ is the angle formed by the anomalous Keller's cone with the edge direction $\hat{\mathbf{e}}$, and is different from the incidence angle $\beta'$, in accordance with (24); $\phi^d$ defines the observation angle on the anomalous Keller's cone, projected on the transverse plane to the edge, while $\phi'^r$ is the transverse angle defining the specular direction of $\hat{\mathbf{s}}_r$ (see Fig. 4) so that the diffraction coefficient exhibits its transition at the ARSB, i.e., when $\phi^d + \phi'^r = \pi$ or $\phi^d + \phi'^r = 3\pi$.

The ISB condition is $|\phi - \phi'| = \pi$ and is unchanged w.r.t. the standard UTD.

Of course, if the RIS has a specular radiation mode, this gives rise to a standard UTD diffraction, where all the diffracted rays lay on the ordinary Keller's cone, i.e., $\beta = \beta'$, and the ARSB becomes the ordinary Reflection Shadow Boundary (RSB), i.e., $\phi^d = \phi$ and $\phi'^r = \phi'$.

In the standard UTD from a wedge, the diffraction coefficient is formed by two couples of cotangent terms (one for each face of the wedge), that maximize the coefficient on the ISB and on the RSB, respectively. However, since a RIS is a diffracting half-plane, each couple of cotangents degenerates into a single secant term [17]. Moreover, in the case of a RIS these secant terms are not summed together to form a single coefficient as in standard UTD, as they are applied separately to diffracted rays that belong to different Keller's cones.

Therefore, for a RIS properly designed in order to have a single significant (anomalous) reradiation mode, while the other propagating modes including the specular one are negligible, the scalar UTD coefficients to be used in (28), (29) are expressed by

$$D^i = \frac{-e^{-j\pi/4}}{2\sqrt{2\pi k_0}\sin\beta'} \frac{F\left[k_0 L^i a\left(\phi - \phi'\right)\right]}{\cos\left[(\phi - \phi')/2\right]} \tag{37}$$

$$D^r_{s,h} = \mp \frac{-e^{-j\pi/4}}{2\sqrt{2\pi k_0}\sin\beta} \frac{F\left[k_0 L^r a\left(\phi^d + \phi'^r\right)\right]}{\cos\left[\left(\phi^d + \phi'^r\right)/2\right]} \tag{38}$$

where

$$F(X) = 2j\sqrt{X}\, e^{jX} \int_{\sqrt{X}}^{\infty} e^{-ju^2}\, du \tag{39}$$

is the UTD Fresnel Transition function, with arguments

$$a\left(\phi \pm \phi'\right) = 2\cos^2\left(\frac{\phi \pm \phi'}{2}\right) \tag{40}$$

**Algorithm 1** Computation of the RIS Reradiated Field

```
Read TX information
Define RX grid
for k ← 1 to N_tiles do
    Calculate incident field E^i on tile k
    for n ← 1 to N_modes do
        Use (13) to find the reradiation direction
        Intersect the reradiated beam with the RX grid
        Compute the SMC Γ on tile k using (15)
        Calculate curvature matrix using (21)
        Calculate reflected field E^r for mode n using (23)
        Add ray contribution to total field at RX
    end for
    if tile k is a "border tile" then
        Calculate incident field on the tile edge
        for n ← 1 to N_modes do
            Find the anomalous Keller's cone with (24)
            Intersect Keller's cone with the RX grid
            Calculate UTD coefficient using (29)
            Calculate ρ^d using (26)
            Calculate diffr. field E^d for mode n using (25)
            Add ray contribution to total field at RX
        end for
        Find the ordinary Keller's cone with (27)
        Intersect Keller's cone with the RX grid
        Calculate UTD coefficient using (28)
        Calculate diffracted field E^d using (25)
        Add ray contribution to total field at RX
    end if
end for
```

and distance parameters

$$L^i = \frac{s\left(\rho^i_e + s\right)\rho^i_1\rho^i_2}{\rho^i_e\left(\rho^i_1 + s\right)\left(\rho^i_2 + s\right)} \sin^2\beta' \tag{41}$$

$$L^r = \frac{s\left(\rho^d + s\right)\rho^r_1\rho^r_2}{\rho^d\left(\rho^r_1 + s\right)\left(\rho^r_2 + s\right)} \sin^2\beta. \tag{42}$$

In (41), $\rho^i_1, \rho^i_2$ are the principal curvature radii of the incident wave, while $\rho^i_e$ is the curvature radius of the incident wave on the edge-fixed incidence plane (see Fig. 2).

Instead, in (42) $\rho^r_1, \rho^r_2$ are the principal curvature radii of the reflected wave, computed through (21), while $\rho^d$ is the edge-caustic distance, computed through (26). In the small argument limit $F(X \to 0) \simeq \sqrt{j\pi X}$, it is easy to verify that the factor $\sqrt{L^{i,r}}$ transforms the diffracted field spreading factor into the GO one. As a consequence, the distance parameters in (41), (42) ensure that, at the relevant SB where the arguments (40) vanish, the edge diffracted field exhibits a jump discontinuity compensating the GO abrupt disappearance, thus providing a continuous total field across the SB. This property of the standard UTD is here suitably extended to the ARSB.

As a last remark, it must be noted that the diffraction coefficients (37), (38) apply to different diffracted rays (ordinary and anomalous) that originate from the same point $Q_E$ on the edge, and the corresponding diffracted fields also have different spreading factors and propagate in different directions, which

corresponds to a forward ray-tracing perspective. Therefore, the diffraction coefficients cannot be summed, unlike in standard UTD. Conversely, by assuming a backward ray-tracing perspective, a fixed observation point $P$ in the space might be hit by diffracted rays that originate at two different diffraction points (or "critical points") on the edge [30], i.e., those points which satisfy (24) and (27). In such a case, the total diffracted field in $P$ is expressed by

$$\mathbf{E}^d_{TOT}(P) = \underline{\mathbf{D}}^i \cdot \mathbf{E}^i(Q_{E1}) \sqrt{\frac{\rho^i_e}{s_1\left(\rho^i_e + s_1\right)}}\, e^{-jk_0 s_1} + \underline{\mathbf{D}}^r \cdot \mathbf{E}^i(Q_{E2}) \sqrt{\frac{\rho^d}{s_2\left(\rho^d + s_2\right)}}\, e^{-jk_0 s_2} \quad (43)$$

where $s_1$, $s_2$ are the distances between the critical points $Q_{E1}$, $Q_{E2}$ and the observation point $P$, respectively, and $\rho^d$, $\underline{\mathbf{D}}^i$, $\underline{\mathbf{D}}^r$ are computed using (26), (28), and (29). If the RIS has multiple reradiation modes, additional critical points arise, and additional terms of anomalous diffraction are added to (43).

### D. Computation of the Overall Reradiated Field

The procedure for the computation of the reradiated field from a finite-size RIS using the proposed ray approach is summarized in Algorithm 1. The RIS is first subdivided into tiles, and the procedure is iterated over the different tiles and over the different RIS reradiation modes: finally, the reflected and diffracted fields are coherently summed to get the overall reradiated field.

## III. Application Examples

As a first simple benchmark case, we consider a "perfect" anomalous reflector [23], [31], illuminated with a plane wave at normal incidence. The RIS has size $7 \times 7$ m$^2$, is centered in the origin of an orthogonal reference system $Oxyz$, and lays on the $xy$ plane. Furthermore, the RIS is designed for an anomalous reflection angle $\theta_r = 60°$, and a normal incident wave with perpendicular (TE) polarization with respect to the $xz$ plane, at the frequency of 3.5 GHz. This can be accomplished by setting the following expressions in the SMC coefficient (15):

$$\chi^m = k_0(\sin\theta_i - \sin\theta_r)x$$
$$A^m = \sqrt{\cos\theta_i / \cos\theta_r}$$
$$\underline{\mathbf{R}}^m = \hat{\mathbf{y}}\hat{\mathbf{y}}.$$

This means that the RIS imposes a constant phase gradient $\nabla\chi^m = k_0(\sin\theta_i - \sin\theta_r)\hat{\mathbf{x}}$ along the $x$ axis, the wave polarization is perpendicular to the reradiation plane and is not altered by the RIS, while the term $A^m = \sqrt{\cos\theta_i / \cos\theta_r}$ accounts for global power conservation [31]. Such kind of "perfect" anomalous reflector with a single reradiation mode and global power conservation requires a nonlocal design of the surface impedance through excitation of additional auxiliary evanescent fields or by carefully engineering the surface reactance profile, and can be achieved for example with a nonuniform array of metal patches separated by a dielectric layer from a ground plane, as described in [23].

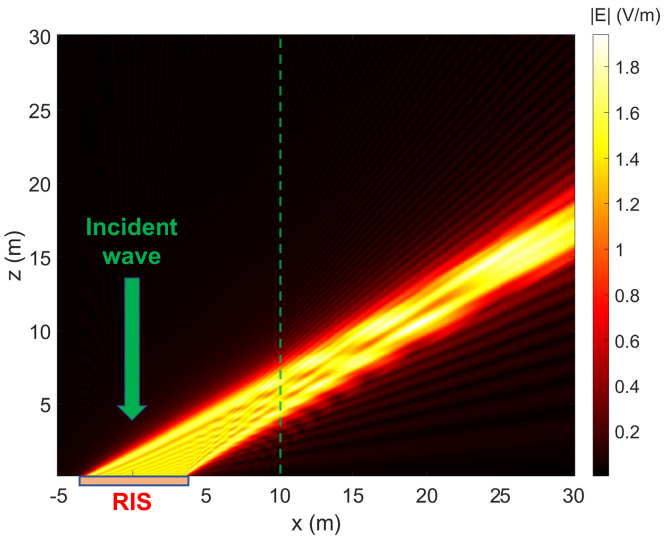


Fig. 5. Field distribution for a perfect anomalous reflector, with $\theta_i = 0°$, $\theta_r = 60°$. Frequency: $f = 3.5$ GHz. TE-polarized incident plane wave, with $|\mathbf{E}^i| = 1$ V/m at the RIS surface.

In Fig. 5, the distribution of the reradiated E-field computed with the ray model on the $xz$ plane is shown, assuming a unitary incident field $\mathbf{E}^i = (-1\ V/m)\hat{\mathbf{y}}$ at the RIS surface. Being an high-resolution image, interference fringes caused by edge diffraction are well visible, both inside and outside the reflection cone. The result of Fig. 5 is very similar to the one shown in [13, Fig. 4] except for a small scale factor in the values of the reradiated field, as this previous result was obtained using a different model, called "Antenna Array-Like" (AAL) model, and applied to the case of an *ideal* phase-gradient reflector, by using a "locally-specular" reflection assumption, which can cause a small bias error, as mentioned in [13].

In order to show the effectiveness of the proposed approach, the scattered field computed with the ray model and shown in Fig. 5 is compared with the one computed using the Physical Optics approach, which is well-proven and widely used [10]. The PO field is computed through the following radiation integral:

$$\mathbf{E}^s_{PO}(\mathbf{r}) = -\frac{jk_0}{4\pi}\int_S \frac{e^{-jk_0|\mathbf{r}-\mathbf{r}'|}}{|\mathbf{r}-\mathbf{r}'|}\left[\eta\,\hat{\mathbf{r}}\times\mathbf{J}_S(\mathbf{r}')\times\hat{\mathbf{r}} + \mathbf{M}_S(\mathbf{r}')\times\hat{\mathbf{r}}\right]dS \quad (44)$$

where the equivalent surface currents for an impenetrable metasurface are approximated as [10]

$$\mathbf{J}_S = \hat{\mathbf{n}} \times \left(\mathbf{H}^i + \mathbf{H}^r\right)$$
$$\mathbf{M}_S = -\hat{\mathbf{n}} \times \left(\mathbf{E}^i + \mathbf{E}^r\right) = -\hat{\mathbf{n}} \times \left(\mathbf{E}^i + \underline{\Gamma}\ \mathbf{E}^i\right) \quad (45)$$

with

$$\mathbf{H}^{i,r} = \frac{1}{\eta}\hat{\mathbf{s}}^{i,r} \times \mathbf{E}^{i,r}. \quad (46)$$

By comparing the whole predicted field in Fig. 5 with the one obtained using the PO model on the same Rx grid, one obtains that the root mean square (rms) distance between the two models is about 2.1% of the unit incident field. The reference PO solution is obtained through numerical

TABLE I
ACCURACY AND COMPUTATION TIME OF RAY MODEL AND AAL MODEL WITH RESPECT TO THE REFERENCE PO MODEL

| Model | Mean error | Error std deviation | RMS error | Computation time (s) |
|---|---|---|---|---|
| PO model | — | — | — | 63918 |
| AAL model | 0.19% | 1.33% | 1.35% | 8767 |
| Ray model | 0.16% | 2.07% | 2.08% | 200 |

computation of the integral (44) with a discretization of the RIS into tiles of length $\lambda/2$, the minimum resolution to have a reliable prediction without grating lobes [13]. It is worth noting that both the ray and the PO solutions are slightly approximate, albeit in different ways, the first being based on an asymptotic approximation of the field for high frequencies, and the second on the assumption that the total field is zero on the shadow side of the RIS and the radiating currents are not perturbed near the edges. However, the ray-based approach is intrinsically more efficient. Just to have an idea, to produce the high-resolution image of Fig. 5 (1.2 Mpixel) with numerical solution of the integral (44), using MATLAB on a workstation with Intel[1] Xeon[1] E5-2620 CPU and parallelization on 8 cores, it takes about 17 h and 45 min. On the contrary, the same result can be obtained with the ray model in about 200 s. Results are summarized in Table I in terms of mean error, standard deviation of the error, and rms error with respect to the reference PO model, and computation time. The errors are expressed as a percentage of the unit incident field. Table I also reports the AAL model of [13], which has intermediate performance: the mean error is slightly worse and the error standard deviation is slightly better than the ray model, but its computation time is of about 2 h and 26 min, which is 43 times slower than the ray model.

In order to provide a visual comparison between the proposed ray model and the PO reference model, the reradiated field shown in Fig. 5 is sampled along the RX line at $x = 10$, $y = 0$ (green dashed line) and compared with the one obtained using the PO model in the same Rx locations. The comparison is shown in Fig. 6 where the reradiated field obtained through the ray model is represented by the black curve, while red dotted curve corresponds to the PO model. The AAL is not plotted in this case for readability reasons, as the curves are very close to each other. It is evident that the 2 curves in Fig. 6 are nearly coincident, thus confirming the validity of the adopted approach. The only small difference that can be appreciated, at $z = 7$, is due to the absence in the model of vertex diffraction, which would allow for a smoother transition when edge ray diffraction ceases to exist.

Anomalous reflectors are usually conceived and designed for the canonical case of an incident plane wave from a given direction, but in a real environment, the incident wave is spherical (or astigmatic), unless the illuminating source is very far. This fact causes an impact on RIS performance, as depicted in Fig. 7, where the same RIS of the previous example is considered (perfect anomalous reflector) and the field along the green dashed line in Fig. 5 is computed with the ray model for an illuminating spherical source located along

[1]Registered trademark.

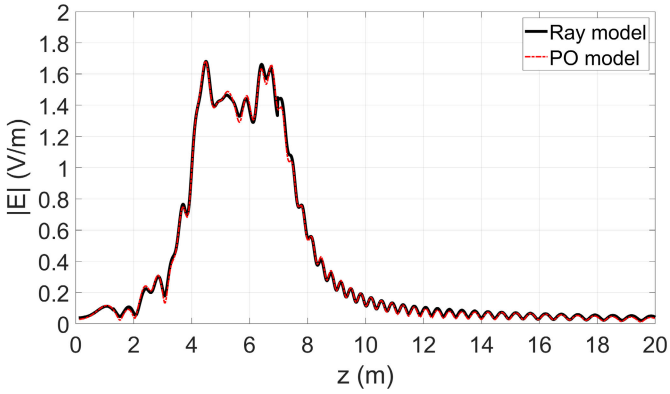


Fig. 6. Comparison of the ray model with the PO model along the dashed green line in Fig. 5.

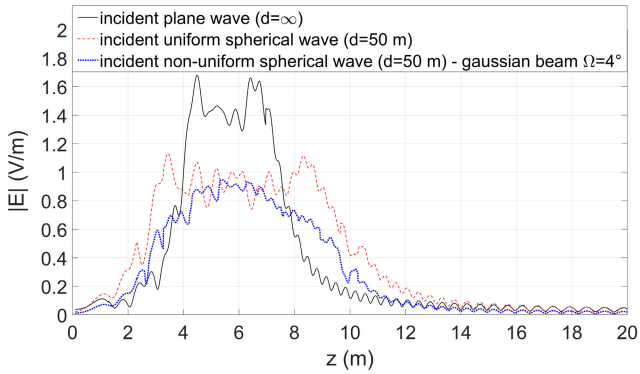


Fig. 7. Comparison of the reradiated field predicted with the ray model along the dashed green line in Fig. 5 in 3 different cases: 1) incident plane wave (black line); 2) incident uniform spherical wave (red dashed line); and 3) incident nonuniform spherical wave with gaussian profile and divergence $\Omega = 4°$ (blue dotted line).

the $z$-axis, at a distance of 50 m from the RIS center. The incident field is normalized so that its maximum value, at the center of the RIS, is 1 V/m. Fig. 7 shows a significant widening of the reflection cone and a reduction in the amplitude of the reradiated field for a uniform spherical incident wave (red dashed curve) compared to the reference case of plane wave illumination (black curve). This is mainly due to the fact that the incidence phase gradient is not constant along the RIS surface, and then the phase compensation operated by the RIS is imperfect. Moreover, the reflected wave is astigmatic, as discussed in Section II, and therefore attenuates faster with distance than a spherical wave.

The reradiated field intensity is further reduced if the RIS is illuminated with a directive antenna. As a reference example, Fig. 7 depicts the case of illumination with a circular gaussian beam (blue dotted curve), that can well approximate the main radiation lobe of a pencil-beam directive antenna [32]. The considered gaussian beam has beam waist $w_0 = 0.39$ m, corresponding to a divergence angle $\Omega = (\lambda/\pi w_0) \approx 4°$ at $f = 3.5$ GHz. As the distance from the source ($d = 50$ m) is far beyond the Rayleigh distance, the incident wave on the RIS surface is a nonuniform spherical wave, and about 86% of its power is contained on a circular spot with radius $R = \Omega d \approx 3.5$ m [33]. As expected, in this case, the reradiated field intensity further decreases compared to the case of incident uniform spherical wave (red dashed curve),

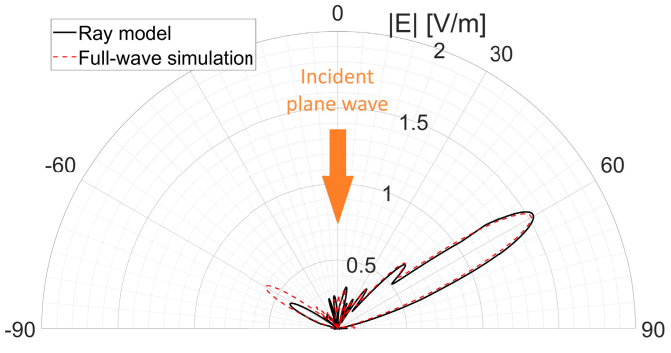


Fig. 8. Comparison between ray model and full-wave simulation along a semicircle on the $xz$ plane centered on the RIS, at a distance $r = 1$ m.

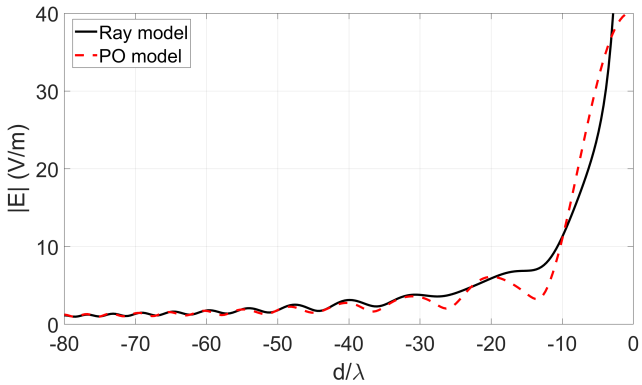


Fig. 9. Comparison between the ray model and the PO model in the case of an ideal focalizing reflector. The distance from the focus is normalized with respect to the wavelength.

especially in the side regions of the reflection cone, where the reduction is of about 6 dB: in fact, since most of the incident power is concentrated around the RIS center, the contribution of edge diffraction becomes less significant in this case.

Fig. 8 shows a more realistic case of a periodic phase-gradient RIS with multiple propagating modes. The ray model is compared with full-wave simulations performed with the frequency-domain solver (FEM) of CST microwave studio. Similar to the previous cases, we consider the reference case of a normally incident plane wave, with field amplitude $E_0 = 1$ V/m on the RIS surface. The RIS is located in the $xy$ plane, centered at the origin, and consists of a reactive impedance sheet $Z_s(x) = j\eta \tan((\pi x/D))$ with period $D$ along the $x$ axis, while the incident field is TE-polarized (i.e., along the $y$ axis). The period can be found as $D = \lambda/|\sin\theta_i - \sin\theta_r|$, in accordance with [10], [23]: therefore, it is chosen as $D = 98.91$ mm in order to give a reflection angle $\theta_r = 60°$ on the $xz$ plane at $f = 3.5$ GHz. To limit the computation time, the size of the RIS in the CST simulation was chosen to be $7D \times 7D$, i.e., about $0.7 \times 0.7$ m$^2$. The surface impedance profile was sampled at 20 points in each period so that the RIS model consists of 140 strips of length $7D$ and width $(D/20)$, each with a constant surface impedance boundary condition. The reradiated field is sampled along a semicircle in the $xz$ plane at a distance $r = 1$ m from the center of the RIS.

In order to compare the full-wave simulation with the ray model, the amplitude and initial phase for the propagating modes have been obtained by first simulating in CST a single periodic cell of the RIS with periodic boundary conditions and Floquet port excitation. According to the Floquet theory, in the considered case of a normally incident plane wave, there are three scattered propagating modes $n = -1, 0, 1$ [10]: $n = 1$ corresponds to the desired reradiation mode at $\theta = 60°$, while $n = 0$ and $n = -1$ correspond to the specular mode ($\theta = 0°$) and to the opposite mode at $\theta = -60°$, respectively. The S-parameters calculated by CST directly provide the amplitude $A^m$ and phase $\chi^m$ of the scattered modes which are used in (15) to obtain the SMC $\underline{\Gamma}$ for each mode. Then, the procedure described in Section II is iterated to obtain the total reradiated field for each of the 3 propagating modes, and such fields are coherently summed to obtain the result shown in Fig. 8 (black curve), which is compared with the reference full-wave simulation (red dashed curve). In both curves, the 2 lobes at $\theta = 60°$ and $\theta = -60°$ are clearly visible, whereas the specular mode appears to be almost negligible, except for a few grating lobes. It is apparent that the proposed ray-method can predict the RIS scattering with good accuracy. Overall, the rms distance between the 2 curves is equal to 0.019, i.e., 1.9% of the unit incident field. The direction and level of the main lobes are quite well estimated except for the underestimation of the lobe at $\theta = -60°$ corresponding to the mode $n = -1$. Such a difference is due to the fact that the ray-method is based on the PO currents, i.e., on the equivalent currents in the infinite periodic problem, which are only an approximation of the true currents on the truncated structure calculated by the full-wave method. As the difference between the two currents is mainly concentrated at the plate edges, the edge diffraction as predicted under the PO approximation may differ from exact edge diffraction. However, such a difference generally decreases as the electrical size of the RIS increases. In this moderate-size example it is still noticeable, though not dramatic.

As a last example, we consider an *ideal* focalizing reflector, illuminated by a TE-polarized plane wave with $|\mathbf{E}^i| = 1$ V/m and incidence angle $\theta_i = \pi/3$ on the $xz$ plane, at the frequency $f = 3.5$ GHz: this is achieved by setting $A^m = 1$ and $\chi^m = -\chi^i + k_0|\mathbf{r}_F - \mathbf{r}'|$ in (15), where $\chi^i = -k_0 \sin\theta_i\, x$ is the phase of the incident wave and $\mathbf{r}_F$ is the position vector of the focus point [13]. The RIS has the same size as the one considered in the example of Fig. 5, and it is centered in the point $(0, 0, -10)$, while the focus point is located in the origin of the reference system.

Fig. 9 shows the predicted field along the z-axis, starting from the RIS surface up to the focus point, and compares the proposed ray model with the PO model. In the plot, the distance from the focus is normalized to the wavelength, to give a clear idea of the focal-spot size that must be related to the wavelength (radius of about $5\lambda$). Recalling that the GO field has singularities on caustics (or focii), as mentioned in Section II, it can be observed that the ray model provides reliable results and in good agreement with the PO model up to a distance of about $5\lambda$ from the focus, then the predicted field value starts diverging. Proper handling of singularities in focal points will have to be addressed in future work, together with the introduction of vertex diffraction and extension of the model to transmissive surfaces.

## IV. Conclusion

On the base of the characterization of a finite-size, reflective RIS through a "spatial modulation" dyadic function and a few parameters, in the present work we propose a fully ray-based approach for the computation of the reradiated field that can be easily embedded in efficient, forward ray tracing algorithms. The model is based on the computation of the anomalous direction of the reflected or diffracted ray based on the phase gradient of the spatial modulation function, and on the computation of its spreading factor using the curvature matrix of the local wavefront. We show that a new Keller's cone, the "anomalous Keller cone," has to be taken into account in addition to the ordinary one and a new, original formulation of the UTD diffraction coefficients is proposed inspired by the heuristic approach in [27] and [28]. We validate the proposed model by comparison to well-established methods available in the literature: results show that the ray model is far more efficient in terms of computation time, but corresponding results are very similar in a number of benchmark cases.

## Appendix I
## Anomalous Reflection: Computation of the Wave Curvature Matrix

Let's consider a reference point $P_0$ on the RIS surface, and the corresponding position vector $\mathbf{r}'_0$. The phase of the incident ray in a point $P$ with position vector $\mathbf{r}'$ located in the vicinity of $P_0$ can be approximated by its Taylor series expansion about $P_0$, truncated after the second-order term

$$\psi^i(\mathbf{r}') \simeq \psi^i(\mathbf{r}'_0) + \hat{\mathbf{s}}^i(\mathbf{r}'_0)\cdot[\mathbf{r}'-\mathbf{r}'_0] + \frac{1}{2}[\mathbf{r}'-\mathbf{r}'_0]\cdot\left\{\underline{\mathbf{Q}}^i(\mathbf{r}'_0)[\mathbf{r}'-\mathbf{r}'_0]\right\} \quad (47)$$

where the identities $\nabla\psi^i \equiv \hat{\mathbf{s}}^i$ and $\nabla\nabla\psi^i \equiv \underline{\mathbf{Q}}^i$ have been used, as stated in Section II-A.

Similarly, the phase of the reflected field can be locally approximated as

$$\psi^r(\mathbf{r}') \simeq \psi^r(\mathbf{r}'_0) + \hat{\mathbf{s}}^r(\mathbf{r}'_0)\cdot[\mathbf{r}'-\mathbf{r}'_0] + \frac{1}{2}[\mathbf{r}'-\mathbf{r}'_0]\cdot\left\{\underline{\mathbf{Q}}^r(\mathbf{r}'_0)[\mathbf{r}'-\mathbf{r}'_0]\right\}. \quad (48)$$

The same principle also applies to the phase $\chi^m$ imposed by the RIS

$$\chi^m(\mathbf{r}') \simeq \chi^m(\mathbf{r}'_0) + \nabla\chi^m(\mathbf{r}'_0)\cdot[\mathbf{r}'-\mathbf{r}'_0] + \frac{1}{2}[\mathbf{r}'-\mathbf{r}'_0]\cdot\{\nabla\nabla\chi^m(\mathbf{r}'_0)[\mathbf{r}'-\mathbf{r}'_0]\}. \quad (49)$$

For a generic surface, any point $P$ in the vicinity of $P_0$ is described by the following relation [20]:

$$\mathbf{r}' = \mathbf{r}'_0 + \mathbf{t} - \frac{1}{2}\left(\mathbf{t}\cdot\underline{\mathbf{C}}\mathbf{t}\right)\hat{\mathbf{n}} \quad (50)$$

where $\mathbf{t} = t_1\hat{\mathbf{u}} + t_2\hat{\mathbf{v}}$ is a vector tangent to the surface in $\mathbf{r}'_0$ and $\mathbf{C} = \kappa_1\hat{\mathbf{u}}\hat{\mathbf{u}} + \kappa_2\hat{\mathbf{v}}\hat{\mathbf{v}}$ is the curvature matrix of the surface. However, in the present work, we are considering only flat surfaces ($\mathbf{C} = \mathbf{0}$), so $\mathbf{r}' - \mathbf{r}'_0$ will be a tangent vector to the surface, i.e.,

$$\mathbf{r}' - \mathbf{r}'_0 = \mathbf{t}. \quad (51)$$

By imposing the phase matching relation (18b) in the point P, we have then

$$\psi^r(\mathbf{r}'_0) + \hat{\mathbf{s}}^r\cdot\mathbf{t} + \frac{1}{2}\mathbf{t}\cdot\underline{\mathbf{Q}}^r\mathbf{t} = \psi^i(\mathbf{r}'_0) + \hat{\mathbf{s}}^i\cdot\mathbf{t} + \frac{1}{2}\mathbf{t}\cdot\underline{\mathbf{Q}}^i\mathbf{t} - \frac{1}{k_0}\left\{\chi^m(\mathbf{r}'_0) + \nabla\chi^m(\mathbf{r}'_0)\cdot\mathbf{t} + \frac{1}{2}\mathbf{t}\cdot\left[\nabla\nabla\chi^m(\mathbf{r}'_0)\mathbf{t}\right]\right\} \quad (52)$$

and then, the following equations must be separately satisfied:

$$\psi^r(\mathbf{r}'_0) = \psi^i(\mathbf{r}'_0) - \frac{1}{k_0}\chi^m(\mathbf{r}'_0) \quad (53a)$$

$$\hat{\mathbf{s}}^r\cdot\mathbf{t} = \left[\hat{\mathbf{s}}^i - \frac{1}{k_0}\nabla\chi^m(\mathbf{r}'_0)\right]\cdot\mathbf{t} \quad (53b)$$

$$\mathbf{t}\cdot\underline{\mathbf{Q}}^r\mathbf{t} = \mathbf{t}\cdot\left\{\left[\underline{\mathbf{Q}}^i - \frac{1}{k_0}\nabla\nabla\chi^m(\mathbf{r}'_0)\right]\mathbf{t}\right\}. \quad (53c)$$

Equation (53a) just provides the phase matching on the reference position $\mathbf{r}'_0$. Equation (53b) means that the tangent components of the first-order terms of Taylor's expansion are equal, as (53b) must be satisfied for any choice of the vector $\mathbf{t}$. So, using the projection operator $\underline{\mathbf{P}}_\tau = \underline{\mathbf{1}} - \hat{\mathbf{n}}\hat{\mathbf{n}}$ we get (12)

$$\underline{\mathbf{P}}_\tau\hat{\mathbf{s}}^r = \underline{\mathbf{P}}_\tau\left[\hat{\mathbf{s}}^i - \frac{1}{k_0}\nabla\chi^m(\mathbf{r}'_0)\right] = -\frac{\nabla\chi^i(\mathbf{r}'_0) + \nabla\chi^m(\mathbf{r}'_0)}{k_0} = -\frac{\nabla\chi(\mathbf{r}'_0)}{k_0}$$

which leads to (13) by imposing $|\hat{\mathbf{s}}^r| = 1$.

Finally, by pre-multiplying and post-multiplying with the projection operator the second-order terms (curvature matrices) in (52), we immediately get (20)

$$\underline{\mathbf{P}}_\tau\underline{\mathbf{Q}}^r\underline{\mathbf{P}}_\tau = \underline{\mathbf{P}}_\tau\left[\underline{\mathbf{Q}}^i - \frac{1}{k_0}\nabla\nabla\chi^m\right]\underline{\mathbf{P}}_\tau$$

which leads to (21) by imposing $\underline{\mathbf{Q}}^r\hat{\mathbf{s}}^r = \mathbf{0}$.

## Appendix II
## Anomalous Diffraction: Computation of the Wave Curvature $\rho^d$

We proceed in a similar way as for reflection, by writing the Taylor series expansion of the phase functions of the incident and diffracted wave, respectively, about a point $P_0$ on the edge

$$\psi^i(\mathbf{r}') \simeq \psi^i(\mathbf{r}'_0) + \hat{\mathbf{s}}^i\cdot(\mathbf{r}'-\mathbf{r}'_0) + \frac{1}{2}(\mathbf{r}'-\mathbf{r}'_0)\cdot\left\{\underline{\mathbf{Q}}^i(\mathbf{r}'_0)[\mathbf{r}'-\mathbf{r}'_0]\right\} \quad (54)$$

$$\psi^d(\mathbf{r}') \simeq \psi^d(\mathbf{r}'_0) + \hat{\mathbf{s}}^d\cdot(\mathbf{r}'-\mathbf{r}'_0) + \frac{1}{2}(\mathbf{r}'-\mathbf{r}'_0)\cdot\left\{\underline{\mathbf{Q}}^d(\mathbf{r}'_0)[\mathbf{r}'-\mathbf{r}'_0]\right\} \quad (55)$$

and similarly for the phase profile $\chi^m$ imposed by the RIS

$$\chi^m(\mathbf{r}') \simeq \chi^m(\mathbf{r}'_0) + \nabla\chi^m(\mathbf{r}'_0)\cdot(\mathbf{r}'-\mathbf{r}'_0) + \frac{1}{2}(\mathbf{r}'-\mathbf{r}'_0)\cdot\{\nabla\nabla\chi^m(\mathbf{r}'_0)[\mathbf{r}'-\mathbf{r}'_0]\}. \quad (56)$$

As we assume that the edge is rectilinear, we have

$$\mathbf{r}' - \mathbf{r}'_0 = ds\ \hat{\mathbf{e}} \tag{57}$$

and then, by imposing the *phase matching* relation

$$\psi^d(\mathbf{r}') = \psi^i(\mathbf{r}') - \frac{1}{k_0}\chi^m(\mathbf{r}') \tag{58}$$

e by substituting (54)–(57) into (58), we get

$$\begin{aligned}&\psi^i(\mathbf{r}'_0) + \hat{s}^i \cdot \hat{\mathbf{e}}\ ds - \frac{\nabla\chi^m(\mathbf{r}'_0)}{k_0} \cdot \hat{\mathbf{e}}\ ds \\ &\quad + \frac{1}{2}\left[\hat{\mathbf{e}} \cdot \underline{\mathbf{Q}}^i(\mathbf{r}'_0)\hat{\mathbf{e}}\right]ds^2 - \frac{1}{k_0}\left[\hat{\mathbf{e}} \cdot \nabla\nabla\chi^m(\mathbf{r}'_0)\hat{\mathbf{e}}\right]ds^2 \\ &= \psi^d(\mathbf{r}'_0) + \hat{\mathbf{s}}^d \cdot \hat{\mathbf{e}}\ ds + \frac{1}{2}\left[\hat{\mathbf{e}} \cdot \underline{\mathbf{Q}}^d(\mathbf{r}'_0)\hat{\mathbf{e}}\right]ds^2.\end{aligned} \tag{59}$$

Finally, by equating separately the zero-order, first-order and second-order terms, we obtain

1) The phase matching in $\mathbf{r}'_0$

$$\psi^i(\mathbf{r}'_0) = \psi^d(\mathbf{r}'_0) \tag{60}$$

2) The *generalized law of diffraction*

$$\hat{\mathbf{s}}^d \cdot \hat{\mathbf{e}} = \cos\beta = \left(\hat{\mathbf{s}}^i - \frac{\nabla\chi^m}{k_0}\right) \cdot \hat{\mathbf{e}} = \cos\beta' - \frac{\nabla\chi^m}{k_0} \cdot \hat{\mathbf{e}} \tag{61}$$

3) The matching of the wave curvatures

$$\hat{\mathbf{e}} \cdot \underline{\mathbf{Q}}^d(\mathbf{r}'_0)\hat{\mathbf{e}} = \hat{\mathbf{e}} \cdot \underline{\mathbf{Q}}^i(\mathbf{r}'_0)\hat{\mathbf{e}} - \frac{1}{k_0}\hat{\mathbf{e}} \cdot \nabla\nabla\chi^m(\mathbf{r}'_0)\hat{\mathbf{e}}. \tag{62}$$

In (62), we observe that $\hat{\mathbf{e}} \cdot \underline{\mathbf{Q}}^i(\mathbf{r}'_0)\hat{\mathbf{e}}$ gives the ray curvature of the incident wave on the edge-fixed incidence plane (i.e., $1/\rho_e^i$), projected along the edge, i.e., multiplied by $\sin^2\beta'$, as the component of the edge direction along the ray gives no contribution, in accordance with (6). Therefore

$$\hat{\mathbf{e}} \cdot \underline{\mathbf{Q}}^i(\mathbf{r}'_0)\hat{\mathbf{e}} = \frac{1}{\rho_e^i}\sin^2\beta' \tag{63}$$

and a similar relation holds for the diffracted wave

$$\hat{\mathbf{e}} \cdot \underline{\mathbf{Q}}^d(\mathbf{r}'_0)\hat{\mathbf{e}} = \frac{1}{\rho^d}\sin^2\beta. \tag{64}$$

Finally, recognizing that $\hat{\mathbf{e}} \cdot \nabla\nabla\chi^m(\mathbf{r}'_0)\hat{\mathbf{e}}$ is the second-order derivative of $\chi^m$ along the edge direction, i.e.,

$$\hat{\mathbf{e}} \cdot \nabla\nabla\chi^m(\mathbf{r}'_0)\hat{\mathbf{e}} \doteq \frac{\partial^2\chi^m}{\partial e^2} \tag{65}$$

and by substituting (63)–(65) into (62) we immediately get (26)

$$\frac{1}{\rho^d} = \frac{1}{\rho_e^i}\frac{\sin^2\beta'}{\sin^2\beta} - \frac{1}{k_0\sin^2\beta}\frac{\partial^2\chi^m}{\partial e^2}.$$

## REFERENCES


[1] M. Di Renzo et al., "Smart radio environments empowered by reconfigurable intelligent surfaces: How it works, state of research, and the road ahead," *IEEE J. Sel. Areas Commun.*, vol. 38, no. 11, pp. 2450–2525, Nov. 2020.

[2] J. Huang et al., "Reconfigurable intelligent surfaces: Channel characterization and modeling," *Proc. IEEE*, vol. 110, no. 9, pp. 1290–1311, Sep. 2022.

[3] M. Di Renzo, F. H. Danufane, and S. Tretyakov, "Communication models for reconfigurable intelligent surfaces: From surface electromagnetics to wireless networks optimization," *Proc. IEEE*, vol. 110, no. 9, pp. 1164–1209, Sep. 2022.

[4] M. Jian et al., "Reconfigurable intelligent surfaces for wireless communications: Overview of hardware designs, channel models, and estimation techniques," *Intell. Converg. Netw.*, vol. 3, no. 1, pp. 1–32, Mar. 2022.

[5] W. Tang et al., "Wireless communications with reconfigurable intelligent surface: Path loss modeling and experimental measurement," *IEEE Trans. Wireless Commun.*, vol. 20, no. 1, pp. 421–439, Jan. 2021.

[6] E. Basar, I. Yildirim, and F. Kilinc, "Indoor and outdoor physical channel modeling and efficient positioning for reconfigurable intelligent surfaces in mmWave bands," *IEEE Trans. Commun.*, vol. 69, no. 12, pp. 8600–8611, Dec. 2021.

[7] Z. Lian, Y. Su, Y. Wang, and L. Jiang, "A non-stationary 3-D wideband channel model for intelligent reflecting surface-assisted HAP-MIMO communication systems," *IEEE Trans. Veh. Technol.*, vol. 71, no. 2, pp. 1109–1123, Feb. 2022.

[8] Y. Liu and C. D. Sarris, "Efficient propagation modeling for communication channels with reconfigurable intelligent surfaces," *IEEE Antennas Wireless Propag. Lett.*, vol. 21, no. 10, pp. 2120–2124, Oct. 2022.

[9] J. Budhu and A. Grbic, "Perfectly reflecting metasurface reflectarrays: Mutual coupling modeling between unique elements through homogenization," *IEEE Trans. Antennas Propag.*, vol. 69, no. 1, pp. 122–134, Jan. 2021.

[10] A. Díaz-Rubio and S. A. Tretyakov, "Macroscopic modeling of anomalously reflecting metasurfaces: Angular response and far-field scattering," *IEEE Trans. Antennas Propag.*, vol. 69, no. 10, pp. 6560–6571, Oct. 2021.

[11] F. H. Danufane, M. Di Renzo, J. De Rosny, and S. Tretyakov, "On the path-loss of reconfigurable intelligent surfaces: An approach based on Green's theorem applied to vector fields," *IEEE Trans. Commun.*, vol. 69, no. 8, pp. 5573–5592, Aug. 2021.

[12] S. Stewart, Y. L. C. de Jong, T. J. Smy, and S. Gupta, "Ray-optical evaluation of scattering from electrically large metasurfaces characterized by locally periodic surface susceptibilities," *IEEE Trans. Antennas Propag.*, vol. 70, no. 2, pp. 1265–1278, Feb. 2022.

[13] V. Degli-Esposti, E. M. Vitucci, M. D. Renzo, and S. A. Tretyakov, "Reradiation and scattering from a reconfigurable intelligent surface: A general macroscopic model," *IEEE Trans. Antennas Propag.*, vol. 70, no. 10, pp. 8691–8706, Oct. 2022.

[14] J. S. Lu et al., "A discrete environment-driven GPU-based ray launching algorithm," *IEEE Trans. Antennas Propag.*, vol. 67, no. 2, pp. 1180–1192, Feb. 2019.

[15] L. Felsen and N. Marcuvitz, *Radiation and Scattering of Waves* (IEEE Press Series on Electromagnetic Wave Theory). Hoboken, NJ, USA: Wiley, 1994.

[16] J. B. Keller, "Geometrical theory of diffraction," *J. Opt. Soc. Amer.*, vol. 52, no. 2, pp. 116–130, 1962.

[17] R. G. Kouyoumjian and P. H. Pathak, "A uniform geometrical theory of diffraction for an edge in a perfectly conducting surface," *Proc. IEEE*, vol. 62, no. 11, pp. 1448–1461, Nov. 1974.

[18] Y. L. C. de Jong, "Uniform ray description of physical optics scattering by finite locally periodic metasurfaces," in *Proc. IEEE Trans. Antennas Propag.*, vol. 70, no. 4, pp. 2949–2959, Apr. 2022.

[19] E. M. Vitucci, J. S. Lu, S. Gordon, J. J. Zhu, and V. Degli-Esposti, "Discrete environment-driven GPU-based ray launching: Validation and applications," *Electronics*, vol. 10, no. 21, p. 2630, 2021. [Online]. Available: https://www.mdpi.com/2079-9292/10/21/2630

[20] G. A. Deschamps, "Ray techniques in electromagnetics," *Proc. IEEE*, vol. 60, no. 9, pp. 1022–1035, Jun. 1972.

[21] G. L. James, *Geometrical Theory of Diffraction for Electromagnetic Waves* (IEE Electromagnetic Waves Series). Stevenage, U.K.: Peregrinus, 1986. [Online]. Available: https://books.google.it/books?id=Xj5ALowljO4C

[22] I. Kay and J. B. Keller, "Asymptotic evaluation of the field at a caustic," *J. Appl. Phys.*, vol. 25, no. 7, pp. 876–883, Jul. 1954.

[23] A. Diaz-Rubio, V. Asadchy, A. Elsakka, and S. Tretyakov, "From the generalized reflection law to the realization of perfect anomalous reflectors," *Sci. Adv.*, vol. 3, no. 8, pp. 1–10, 2017.

[24] C. A. Balanis, *Advanced Engineering Electromagnetics*. Hoboken, NJ, USA: Wiley, 2012.
[25] F. Yang and Y. Rahmat-Samii, *Surface Electromagnetics: With Applications in Antenna, Microwave, and Optical Engineering*. Cambridge, U.K.: Cambridge Univ. Press, 2019.
[26] M. Albani, G. Carluccio, and P. H. Pathak, "Uniform ray description for the PO scattering by vertices in curved surface with curvilinear edges and relatively general boundary conditions," *IEEE Trans. Antennas Propag.*, vol. 59, no. 5, pp. 1587–1596, May 2011.
[27] R. Luebbers, "Finite conductivity uniform GTD versus knife edge diffraction in prediction of propagation path loss," *IEEE Trans. Antennas Propag.*, vol. AP-32, no. 1, pp. 70–76, Jan. 1984.
[28] P. D. Holm, "A new heuristic UTD diffraction coefficient for nonperfectly conducting wedges," *IEEE Trans. Antennas Propag.*, vol. 48, no. 8, pp. 1211–1219, Aug. 2000.
[29] D. McNamara, C. Pistorius, and J. Malherbe, *Introduction to the Geometrical Theory of Diffraction*. Norwood, MA, USA: Artech House, 1990.
[30] F. Capolino, M. Albani, S. Maci, and S. Felsen, "Frequency-domain Green's function for a planar periodic semi-infinite phased array. II. Diffracted wave phenomenology," *IEEE Trans. Antennas Propag.*, vol. 48, no. 1, pp. 75–85, Jan. 2000.
[31] C. Simovski and S. Tretyakov, *An Introduction to Metamaterials and Nanophotonics*. Cambridge, U.K.: Cambridge Univ. Press, 2020.
[32] G. Buttazzoni and R. Vescovo, "Density tapering of linear arrays radiating pencil beams: A new extremely fast Gaussian approach," *IEEE Trans. Antennas Propag.*, vol. 65, no. 12, pp. 7372–7377, Dec. 2017.
[33] O. Svelto, *Principles of Lasers*. New York, NY, USA: Springer, 2012.

**Enrico Maria Vitucci** (Senior Member, IEEE) is currently an Associate Professor in applied electromagnetics, antennas, and propagation with the Department of Electrical, Electronic and Information Engineering "G. Marconi" (DEI), University of Bologna, Bologna, Italy. He was a Research Associate with the Center for Industrial Research on ICT, University of Bologna. In 2015, he was a Visiting Researcher with Polaris Wireless, Inc., Mountain View, CA, USA. He is the Chair of the Cesena-Forli Unit of the Inter-Department Center for Industrial Research on ICT (CIRI-ICT), University of Bologna. He is the author or coauthor of about 100 technical articles on international journals and conferences, and a co-inventor of five international patents. He has participated in several European research and cooperation programs (COST 2100, COST IC1004, COST IRACON, and COST INTERACT) and the European Networks of Excellence NEWCOM and NEWCOM++. His research interests are in deterministic and wireless propagation models for 5G and beyond.

Prof. Vitucci is a member of the Editorial Board of Journal *Wireless Communications and Mobile Computing journal*.

**Matteo Albani** (Fellow, IEEE) received the Laurea degree in electrical engineering and the Ph.D. degree in telecommunications engineering from the University of Florence, Florence, Italy, in 1994 and 1999, respectively.

From 2001 to 2005, he was an Assistant Professor at the University of Messina, Messina, Italy. He is currently Associate Professor with the Department of Information Engineering and Mathematics, University of Siena, Siena, Italy, where he is also the Director of the Applied Electromagnetics Laboratory. He has coauthored more than 80 journal articles more than 200 conference papers, five book chapters, and six patents. His research interests are in the areas of high-frequency methods for electromagnetic scattering and propagation, numerical methods for array antennas, antenna analysis and design, metasurfaces and metamaterials, and inhomogeneous lens antennas.

Dr. Albani is a member of EurAAP, URSI, and SiEM. He received the Best Paper Awards at the XIV RiNEM 2002, URSI EMTS 2004, European AMTA Symposium 2006, URSI EMTS 2010, and EuCAP 2014 and EuCAP 2018.

**Silvi Kodra** received the M.Sc. degree in telecommunications engineering from the University of Bologna, Bologna, Italy, in 2021, and the M.Sc. degree in electronics and communication engineering from Tongji University, Shanghai, China, in 2022. She is currently pursuing the Ph.D. degree in telecommunications engineering with the University of Bologna.

Under a grant from EurAAP, she spent one month of her research activity at Durham University, Durham, U.K., working on THz channel measurements. Her activity is focused on the research topic in reconfigurable intelligent surfaces, channel characterization for mm-wave and sub-THz frequencies, and propagation losses in indoor ennvironments. She participates regularly in COST INTERACT.

**Marina Barbiroli** received the Laurea degree in electronic engineering and the Ph.D. degree in computer science and electronic engineering from the University of Bologna, Bologna, Italy, in 1995 and 2000, respectively.

She is currently an Associate Professor with the Department of Electrical, Electronic and Information Engineering "G. Marconi" (DEI), University of Bologna. Her research interests are on propagation models for mobile communications systems, with focus on wideband channel modeling for 5G systems and beyond. Her research activities include investigation of planning strategies for mobile systems, broadcast systems and broadband wireless access systems, and analysis of exposure levels generates by all wireless systems and for increasing spectrum efficiency. The research activity includes the participation to European research and cooperation programs (COST 259, COST 273 COST2100, COST IC1004, COST IRACON, and COST INTERACT) and in the European Networks of Excellence FP6-NEWCOM and FP7-NEWCOM++.

**Vittorio Degli-Esposti** (Senior Member, IEEE) was a Post-Doctoral Researcher at Polytechnic University (now NYU Tandon School of Engineering), Brooklyn, NY, USA, in 1998, in the group led by Prof. H. L. Bertoni. He was a Visiting Professor at the Helsinki University of Technology (now Aalto University), Espoo, Finland, and Tongji University, Shanghai, China, in 2006 and 2013, respectively. From January 2015 to December 2016, he was the Director of Research at Polaris Wireless Inc., Mountain View, CA, USA. He is a Full Professor with the Department of Electrical, Electronic and Information Engineering "G. Marconi" (DEI), Alma Mater Studiorum, University of Bologna, Bologna, Italy. He has participated in several European research projects, including many European Cooperation Actions (COST), the European Networks of Excellence NEWCOM and NEWCOM++, the Seventh Framework Program IP Project ALPHA, and the Horizon Europe Project 6G-SHINE. He has been the Co-Founder and a Lecturer of the biennial courses for Ph.D. students and researchers "Short Range Radio Propagation" and "Mobile Radio Propagation for 5G and Beyond" of the European School of Antennas (https://www.euraap.org/esoa-courses). He is the author or coauthor of more than 160 peer-reviewed technical articles and a co-inventor of seven international patents in the fields of applied electromagnetics, radio propagation, and wireless systems.

Dr. Degli-Esposti was a recipient of the 2023 EurAAP Propagation Award. He was elected as the Chair of the Propagation Working Group of the European Association on Antennas and Propagation (EuRAAP) and of WG1 of COST Action CA20120 "Interact." He was the Vice-Chair of the European Conference on Antennas and Propagation (EuCAP), editions 2010 and 2011, the Short-Courses and Workshops Chair of the 2015 edition, the Convened Sessions Chair of the 2023 edition, an Invited Speaker at EuCAP 2014 and the International Symposium on Antennas and Propagation (ISAP) 2020, and the Short-Courses Chair of the European Conference on Networks and Communications (EuCNC), in 2020. He was the Chair of the Cesena-Forli Unit of the Inter-Department Center for Industrial Research on ICT (CIRI-ICT) of the University of Bologna. He is an Editor of the IEEE TRANSACTIONS ON VEHICULAR TECHNOLOGY and an Associate Editor of the journal *Radio Science*.

Open Access funding provided by 'Alma Mater Studiorum - Università di Bologna' within the CRUI-CARE Agreement